Journal of Materials Chemistry A

Accepted Manuscript

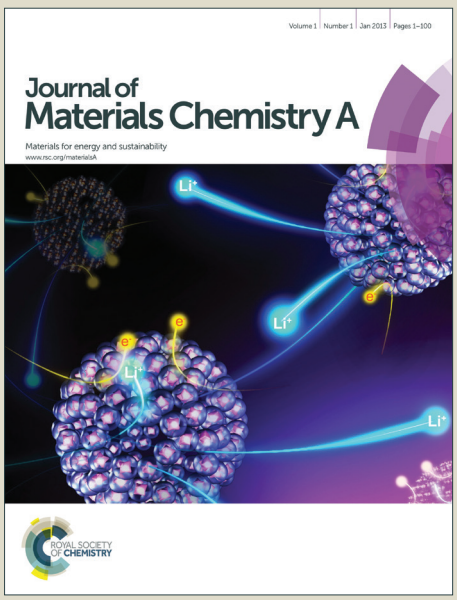

ROYAL SOCIETY OF CHEMISTRY

www.rsc.org/materialsA

Enhanced photovoltaic performance of dye-sensitized solar cells based on Sr-doped $TiO_2/SrTiO_3$ nanorod array heterostructures

Rui Tang, Longwei Yin*

Key Laboratory for Liquid-Solid Structural Evolution and Processing of Materials, Ministry of Education, School of Materials Science and Engineering, Shandong University, Jinan 250061, P. R. China

*To whom correspondence should be addressed. Tel.: + 86 531 88396970. Fax: + 86 531 88396970. E-mail: yinlw@sdu.edu.cn

Abstract We present a novel Sr-doped $TiO_2/SrTiO_3$ nanorod array heterostructures for dye sensitized solar cells (DSSCs) via a facile two-step hydrothermal process, with a tunable microstructure, optical response and photoelectrical conversion properties. The chemical composition components and microstructures of Sr-doped $TiO_2/SrTiO_3$ nanorod array heterostructures are investigated using XRD, XPS, SEM and TEM characterization techniques, respectively. It is shown that the treatment of rutile TiO_2 nanorod arrays in $Sr(NO_3)_2$ solution results in the self-doping of Sr into lattice of TiO_2 and formation of Sr-doped $TiO_2/SrTiO_3$ nanorod array heterostructures, inducing a transition of optical response property from ultraviolet region to visible region. The photogenerated electrons and holes can be effectively separated due to the formation of $SrTiO_3$/Sr-doped TiO_2 heterostructure with uniquely matched band-gap energy structure, resulting in greatly enhanced photoelectric conversion efficiency performance. Electrochemical impedance spectroscopy and photoluminescence results show the formation of Sr-doped $TiO_2/SrTiO_3$ heterostructure can effectively prolong the charge carriers' lifetime. The dye loading capacity on the Sr-doped $TiO_2/SrTiO_3$ heterostructures can be improved through the functionalization bonding of the hydroxide group on surface of the electrode material. DSSCs based on optimized Sr-doped $TiO_2/SrTiO_3$ heterostructure photoanode achieves the highest energy conversion efficiency of 4.70% (one sun illumination), nearly 1.5 times higher than the bare rutile TiO_2 photoanode (3.10%).

Key word: heterostructure; self-doping; $SrTiO_3/TiO_2$; nanorods array; dye sensitized solar cells

1. Introduction

Since great breakthrough in the photoelectric efficiency of dye sensitized solar cell (DSSCs) was made by Graetzel and his collaborators in 1990s,[1] much attention has been focused on DSSCs, which are considered to be one of the most promising solutions to addressing the global energy and environmental pollution crisis.[2] In the past decades, TiO_2 is extensively used as photoanode material because its wide band gap can provide a large open-circuit voltage and well scattering property and improved ability of incident light utilization.[3, 4] TiO_2 has three kinds of phases, anatase, rutile, and brookite phase, among which anatase TiO_2 is mostly used as photoanode, since it is traditionally considered that there exists an inherently higher Fermi level for the anatase than that of the other phases, which may be favorable and preferable to achieve a lower recombination rate for light-induced electron–hole pairs and then a higher open-circuit voltage (V_{OC}) for DSSCs.

However, as an instinct semiconductor, TiO_2 suffers from low quantum efficiency due to rapid recombination of photogenerated electron-hole pairs, which greatly degrades the photo-electrical conversion efficiency in DSSCs and hydrogen production efficiency in water splitting.[5, 6] Furthermore, another drawback of TiO_2 photocatalyst is its optical response only in the ultraviolet region, just a small amount portion of the total sunlight. These are challenging issues as they restrict the high photoelectric performance of TiO_2 based materials.[7, 8] Great efforts have been made to improve the carrier transportation by coupling it with other semiconductors, such as ZnO,[9] SnO_2,[10] Cu_2O,[11] CdS,[12] in order to suppress the electron-hole recombination rates and modify the optical reponse performance. In addition, doping with various metal or nonmetal elements has also been proved to be alternatively effective means to suppress the high recombination rate of photo-induced charges and tune the optical response perfoance.[13-15]

The widely used photoanode for DSSCs is usually based on the TiO_2 nanostructured particles synthesized via a sol-gel process, and then the nanoparticle (NP) TiO_2 layer film is spin-coated onto the FTO glass plates. The NP film always goes through high electron/hole recombination loss since the electron mobility in NP films is about two orders of magnitude lower than that of single crystal due to the electron trapping/scattering at grain boundaries, the more grain boundaries in NP films may result in higher energy loss.[16-19] Such an interface between the spinning-route fabricated TiO_2 NP film and FTO substrate is inevitably not dense, and generally possesses a poor crystallinity, affecting the charge transfer kinetics at the photoanode interface, leading to low electron conductivity and photoelectrical conversion efficiency. To solve this problem, one-dimensional (1D) oriented TiO_2 nanostructures, like nanowire- and nanorod-arrays, can be directly or in-situ grown on FTO substrate to improve the interface stability between TiO_2 layer and the FTO. Recently, it is reported that the electron conductivity of the rutile TiO_2 nanowire-based DSSCs is more than two orders of magnitude higher than that of the spinning coated TiO_2 NP-based DSSCs.[16, 17] The dramatically increased electron transport rate for vertical rutile TiO_2 nanorod arrays relative to nanoparticle-like TiO_2 is presumably associated with the less grain boundaries in nanowire- and nanorod-arrays and more ordered electronic transmission along the oriented structure, and subsequently less energy loss. Some early work proved that better crystallinity and vertically oriented TiO2 nanorods will result in less carrier recombination center and can obviously improve the dye loading, electron diffusion lifetime, and the photoelectric conversion efficiency of DSSCs.[20] Interestingly, for 1D structure, the rutile TiO_2 can achieve an even

higher V_{OC} value and better electron conductivity than anatase phase, which differs from the traditional view mentioned above. Furthermore, rutile TiO_2 has been proved to exhibit additional advantages including better chemical stability, higher refractive index and lower production costs than anatase.[18]

Due to the aforementioned good electron conductivity for rutile TiO_2, 1D rutile TiO_2 nanostructure arrays exhibit promising applications in solar cells,[19, 20] water splitting and photocatalysis,[21-23] the integral photoelectrical conversion performance of DSSCs based on 1D rutile TiO_2 nanostructure is still not satisfied.[23,24] Perovskite-type oxides with a chemical stoichiomety of $MTiO_3$ (M = Ca, Ba, Sr, Pb, etc.), as an important class of functional materials, have been widely investigated for ferroelectric, piezoelectric, and dielectric devices.[24-26] Specially, strontium titanate ($SrTiO_3$), with a unique cubic perovskite structure, has been found to be favorable and catalytically active in photoelectric conversion and water photosplitting because of its outstanding thermal stability and photostability, excellent photocatalytic activity.[27-30] Coupling $SrTiO_3$ with TiO_2 can effectively suppress the carrier recombination through the matched conduction band energy structure (type II cells).[31, 32] It is believed that the matched band structure of the heterostructure materials improves not only the electron transfer from the conduction band of $SrTiO_3$ to that of TiO_2, but also the holes transfer from the valence band of TiO_2 to that of $SrTiO_3$. Currently, several types of $SrTiO_3/TiO_2$ heterostructures applied in photocatalytic, photo watersplitting, and dye sensitized solar cells (DSSCs) have been reported. However, novel Sr-doped $TiO_2/SrTiO_3$ nanorod array heterostructures for DSSCs with a tunable microstructure, optical response performance and photoelectrical conversion properties is full of challenge and seldom reported.

Herein, we present a novel Sr-doped $TiO_2/SrTiO_3$ nanorod array heterostructures for greatly enhanced photoelectric conversion efficiency dye sensitized solar cells (DSSCs) via a facile two-step hydrothermal process. The self-doping of Sr into lattice of TiO_2 and the formation of $SrTiO_3$/Sr-doped TiO_2 heterostructure induces a transition of the optical response from ultraviolet region to visible region. The dye loading capacity on the Sr-doped $TiO_2/SrTiO_3$ nanorod array heterostructures can be improved through the functionalization bonding of the hydroxide group on surface of the electrode material and the carboxyl group of the dye molecule. The photogenerated charge carriers can be effectively separated due to the formation of $SrTiO_3$/Sr-doped TiO_2 heterostructure with uniquely matched bad gap energy structure, which can reduce the probability of recombination of electrons and holes, resulting in greatly enhanced photoelectric conversion efficiency. DSSCs based on Sr-doped $TiO_2/SrTiO_3$ nanorod array heterostructure can achieve a highest short-circuit current density of 8.42 mA cm^{-2} and a maximal photoelectric conversion efficiency of 4.70% under one sun illumination which are 1.31 and 1.51 times larger than pure TiO_2 nanorods, respectively.

2. Experiment details

2.1 preparation of Sr-doped $TiO_2/SrTiO_3$ nanorod heterostructure array.

Synthesis of TiO_2 nanorods array[18, 33]

A typical rutile TiO_2 nanorods array is prepared by a hydrothermal method. Firstly, the FTO glass is cut into small squares (~15 mm×~15 mm) and then cleaned by sonication with deionized water, acetone, and ethanol in turn with each process for 10 min. Sequentially, the cleaned substrates are placed in a Telfon-lined autoclave (80 mL capacity) with a solution of titanium isopropoxide (1.0 ml) in the mixture of hydrochloric acid (30 ml) and

deionized water (30 ml). The vessel is then kept at 150 °C for 8 h. After a cooling process, the substrates are rinsed with deionized water and dried in air.

Preparation of Sr-doped TiO_2/$SrTiO_3$ nanorod heterostrucure [8, 34,32]

The substrates with TiO_2 nanorod array are soaked in a solution with Sr^{2+} ions and converted to Sr-doped TiO_2/$SrTiO_3$ heterostrucure by a further hydrothermal reaction. Typically, the obtained TiO_2 nanorod array is transferred to a new 80 mL of Teflon-lined autoclave, 40% filled with distilled water and 40% filled with NH_4OH solution (26.0wt.%). Then $Sr(NO_3)_2$ powder is added to the autoclave and the concentration of Sr^{2+} is prepared in 5, 25, 50 and 75 mM, respectively (denoted as T1, T2, T3 and T4 respectively). For the bare rutile TiO_2 sample, it is denoted as T0. The autoclave is placed in an electronic oven at 180 °C for 24h. After the hydrothermal process is completed, the nanorods array is collected and sequentially washed with a 0.2 M diluted HCl aqueous solution, water, and ethanol to yield the Sr-doped TiO_2/$SrTiO_3$ nanowire array. Finally, samples are calcined at 600 °C for 30 min to remove the hydroxyl ions.

Hydroxylation Treatment of Photoanode

As-prepared samples are immersed into a mixture of deionized water, ammonium hydroxide and hydrogen peroxide (5/1/1, $V_1/V_2/V_3$) and heated to 80 °C for different time. As treatment is over, the substrates are rinsed with deionized water and ethanol, and then dried at room temperature without any further annealing.

2.2 Solar cell fabrication.

Fabrication of DSSCs. The prepared substrates are scratched into ~0.3 cm × ~0.3 cm pieces and immersed in an acetonitrile solution with 0.3 mM of dye N719 (Cis-diisothocyanato-bis (2,2'-bipyridyl-4,4'-dicarboxylato) ruthenium (II) bis (tetrabutylammonium)) overnight. The excessive N719 dye in the TiO_2 and Sr-doped TiO_2/$SrTiO_3$ heterostructure film was rinsed off with anhydrous ethanol before assembly. The counter electrode is platinized by spraying H_2PtCl_6 solution onto the FTO glass and calcined in air at 410 °C for 20 min. It is then placed directly on the top of the dye-sensitized TiO_2 and Sr-doped TiO_2/$SrTiO_3$ heterostrucure films. The gap between the two electrodes is sealed by thermal adhesive films (Surlyn, Dupont). The electrolyte (electrolyte of 0.6 M 1-methy-3-propylimidazolium iodide (PMII), 0.05 M LiI, 0.05 M I2, and 0.5 M 4-tertbutylpyridine (TBP) in a (85/15, V_1/V_2) mixture of acetonitrile (Aladdin-reagent, China) and valeronitrile (Aladdin-reagent, China)) is filled from a hole made on the counter electrode, which is later sealed by a cover glass and thermal adhesive films.

2.3 Materials characterization.

The microstructure of the species is characterized by XRD (Cu-Kα, 40 kV, 30 mA). All the samples are characterized in the 2θ range of 10-90^o. The morphology and microstructure of samples are characterized by field-emission scanning electron microscopy (FESEM, SU-70) equipped with energy-dispersive X-ray spectroscopy (EDS). High-resolution transmission electron microscopy (TEM, Tecnai 20U-Twin) coupled with selector area electron diffraction (SAED) is used to investigate the crystalline and microsrtrcture details of the samples, operating at 200 kV. X-Ray photoelectron spectroscopy (XPS) measurements of the material binding energy distributions are carried out in a Thermo Scientific ESCALAB250 spectrometer.

The UV-visible diffuse-reflectance spectra and the absorption spectrum are collected from UV-vis spectrophotometry (TU-1900). The dye uptake test is investigated using UV–Vis spectroscopy (TU-1900) by

desorbed the sample film membrane in 0.2 M NaOH water and ethanol (50/50, V_1/V_2) solution. The selected-area electron diffraction (SAED) characterization and microstructural analyses are carried out in a Phillips Tecnai 20U-Twin high-resolution transmission electron microscope at an acceleration voltage of 200 kV. Current–voltage measurements are performed under 1 sun illumination (AM 1.5, 100 mW cm^{-2}) with a Newport solar simulator (Class 3A, 94023A) and a Keithley 2420 source meter equipped with a calibrated Si-reference cell (certificated by NREL). The electrochemical impedance spectra (EIS) are measured with a Princeton Parstate 2273A in a two-electrode design; the sample films served as a working electrode and the Pt-coated ITO or FTO glass as a counter electrode at an applied bias of the open circuit voltage under one-sun irradiation. The frequency range is 10 mHz to 100 KHz; the magnitude of the alternating potential is 20 mV.

3. Result and discussion

3.1 Structure and characterization

Fig. 1 depicts XRD patterns of different samples prepared in $Sr(NO_3)_2$ solution with different concentrations. As shown in Fig. 1a, the profile of pure TiO_2 sample (T0) without treated in $Sr(NO_3)_2$ solution exhibits obvious diffraction peaks of TiO_2 indexed to (101), (111), (210), (211), (002) and (112) planes of tetragonal rutile TiO_2 (JCPDS No. 88-1175) after ignoring the background peaks of FTO. Interestingly, the relative intensity of (002) plane gets stronger, which should be ascribed to the highly [001] oriented growth of TiO_2 nanorod arrays. This evidently demonstrates the successful deposition of rutile TiO_2 nanorod arrays on FTO substrate. Subsequent hydrothermal treatment of the as-prepared TiO_2 nanorod arrays in $Sr(NO_3)_2$ solution is expected to form $SrTiO_3$ on the surface of TiO_2, and the corresponding XRD patterns are presented in Fig. 1a for T1, T2, T3 samples. It is shown that in addition to XRD peaks related to rutile TiO_2, two XRD peaks at 23° and 33° position are observed, which can be indexed to (100) and (110) planes of $SrTiO_3$. Importantly, with the concentration of $Sr(NO_3)_2$ increasing, the intensity of (100) and (110) peaks related to $SrTiO_3$ gets stronger, indicating that the size and content of $SrTiO_3$ increase. The XRD pattern for the magnified (002) peaks synthesized at different $Sr(NO_3)_2$ solution is depicted in Fig. 1b. It should be noted that the (002) peak shifts to the position at small angle with the Sr^{2+} incorporated content increasing, suggesting that the interlayer spacing of (002) gradually expands with the increase of Sr^{2+} concentration. Considering the radium of Sr^{2+} (0.215 Å) is larger than that of Ti^{4+} (0.145 Å), the lattice expansion can be attributed to the substitution of Ti^{4+} by Sr^{2+}. The Sr doping into lattice of TiO_2 can be further confirmed by the following XPS examination, and the doping effect on the optical properties is also further analyzed.

Table 1. Lattice constant of Sr-doped rutile TiO_2 (002) plane

Samples	T0	T1	T2	T3
2θ (°)	62.82	62.80	62.77	62.72
d-spacing (nm)	1.47899	1.47942	1.48006	1.48112

The morphologies of pure TiO_2 and Sr-doped $TiO_2/SrTiO_3$ hetersostructure nanorod arrays are characterized by FESEM, as is shown in Fig. 2. The top view FESEM image in Fig. 2a shows a uniformly distributed nanorod arrays for pure TiO_2 samples, with an average diameter of 150 nm for the TiO_2 nanorods, appearing a regular

square tips resulted from the tetragonal structure of the rutile TiO_2. The cross-sectional FESEM image (Fig. 2b) indicates the nanorod arrays are nearly vertical to the FTO substrate with a thickness of 3.07 μm. After deposition of $SrTiO_3$, the diameter of Sr-doped TiO_2 nanorod gets larger, and the cross-section square tips become less regular. Furthermore, in comparison with pure TiO_2 nanorod arrays, the space between nanorods is mostly filled, evidently indicating the formation of $SrTiO_3$ on the surface of Sr-doped TiO_2 nanorod so as to form the Sr-doped $TiO_2/SrTiO_3$ nanorod hetersostructure arrays (Fig. 2d).

The conversion from TiO_2 to perovskite-type $SrTiO_3$ during the hydrothermal reaction could be nominally expressed in a one-pot reaction:

$$TiO_2 + Sr^{2+} + OH^- \rightarrow SrTiO_3 + H_2O. \quad (1)$$

However, actually, it has been widely considered as a dissolution–precipitation process that involves the dissolution of titanium oxide followed by nucleation of the perovskite $SrTiO_3$. The process can be divided into two steps:

$$TiO_2 + 2OH^- + 2H_2O \rightarrow [Ti(OH)_6]^{2-} \quad (2)$$

$$Sr^{2+} + [Ti(OH)_6]^{2-} \rightarrow SrTiO_3 + 3H_2O \quad (3)$$

Firstly, TiO_2 is dissolved *via* the reaction with OH^- to form $[Ti(OH)_6]^{2-}$ (reaction 2), and then as-formed $[Ti(OH)_6]^{2-}$ reacts with Sr^{2+} to generate $SrTiO_3$ that nucleates on the surface of TiO_2 nanorods (reaction 3). It is noted that the dissolution of TiO_2 and precipitation of $SrTiO_3$ happens on the surface of TiO_2 to form the Sr-doped $TiO_2/SrTiO_3$ nanorod hetersostructure arrays.

To investigate the elemental distribution of Sr-doped $TiO_2/SrTiO_3$ heterostructure, energy-dispersive x-ray spectroscopy (EDS) mapping characterization is performed (T1 sample). As is shown in Fig. 3, it is implied that Ti, Sr, and O elements are homogeneously distributed among the area in Fig. 3a of the cross-sectional FESEM image of Sr-doped $TiO_2/SrTiO_3$ heterostructures.

The microstructures the TiO_2 nanorod (T0) and Sr-doped $TiO_2/SrTiO_3$ nanorod heterostructure (T1) are further revealed by transmission electron microscopy (TEM), as is shown in Fig. 4. According to low magnification TEM image of TiO_2 nanorod sample in Fig. 4a, it is suggested that the products are composed of uniform nanorods with a diameter of around 150 nm, in accordance with the SEM results. Further insight into microstructure of the TiO_2 nanorods is revealed by typical HRTEM lattice image (Fig. 4b). In Fig. 4b, the highlighted inter-spacing of 0.23 nm is well in agreement with that of (200) plane of rutile TiO_2. Fig. 4c shows a typical HRTEM lattice image for the $SrTiO_3$/Sr-doped TiO_2 nanorod heterostructure (T1) sample, small nanoparticles on the surface of Sr-doped TiO_2 nanorods can be revealed. The d-spacing of 0.27 nm corresponds well to that of the (110) plane of $SrTiO_3$. A typical selected area electron diffraction (SAED) pattern is depicted in Fig. 4d (T1). The diffraction rings corresponding well with that of (200), (002) and (112) planes of rutile TiO_2, and (100), (110) planes of $SrTiO_3$, respectively. It is clearly demonstrated that the heterostructure hybrid is composed of rutile Sr-doped TiO_2 and cubic $SrTiO_3$.

More details about the chemical bonding state of the Sr-doped $TiO_2/SrTiO_3$ heterostructure (T1) are investigated by X-ray photoelectron spectroscopy (XPS). From the fully scanned spectra (Fig. 5a), the presence of Sr, Ti, O, C and Sn in the Sr-doped $TiO_2/SrTiO_3$ heterostructure is confirmed. The peak of element Sn is ascribed

to the FTO substrate and the peak of C should be attributed to the carbon-based contaminant, and the binding energy for C 1s at 284.6 eV is used as the reference. According to Liu's work,[33] the Ti related peaks of Ti $2p_{1/2}$ and Ti $2p_{3/2}$ at 464.2 eV and 458.5 eV should be derived from TiO_2 base, respectively. In this regard, two sets of different Ti 2p states can be fitted from Fig. 5b, they are, Ti^{4+}/TiO_2 (Ti $2p_{1/2}$, 464.4 eV; Ti $2p_{3/2}$, 458.6 eV) and Ti^{4+}/$SrTiO_3$ (Ti $2p_{1/2}$, 463.5 eV; Ti $2p_{3/2}$, 457.8 eV). The asymmetry peak of Sr $3d_{5/2}$ around 134.0 eV can be assigned to $SrTiO_3$ and SrO, and SrO is presumed to come from the Sr doping in the lattice of rutile TiO_2 (Fig. 5c).[35] Finally, the peak of O 1s (Fig. 5d) can be assigned to TiO_2, $SrTiO_3$, and SnO_2 resulted from the F-doped SnO_2 substrate as stated before.

3.2 The performance of solar cells

The optical properties of rutile TiO_2 and Sr-doped TiO_2/$SrTiO_3$ heterostructure nanorod array samples are investigated *via* UV–vis diffuse reflectance spectra. Fig. 6a shows the diffuse reflection spectra of the Sr-doped TiO_2/$SrTiO_3$ nanorod array heterostructure and pure TiO_2 nanorod array. According to Guo's work,[14] the Kubelka-Munk function is applied to convert the diffuse reflectance into the equivalent band gap energy.

$$F(R\infty) = (1-R)^2 / (2R) \quad (4)$$

Here, R is the reflectance of the sample. The Fig. 6b shows the plot of $[F(R\infty)hv]^{1/2}$ vs. hv, in which linear segments are extended to intersect with hv-axis to obtain the indirect band gap of the samples. The band gap of Sr-doped TiO_2/$SrTiO_3$ samples with different amount of $SrTiO_3$ is estimated to be 3.02, 2.93, 2.90 and 2.75 eV for T0, T1, T2 and T3 samples, respectively. Interestingly, the Sr-doping into lattice of TiO_2 and formation of Sr-doped TiO_2/$SrTiO_3$ heterostructure could create impurity energy level and modify the optical response property and narrow the band gap for a wide light absorption,[31] which is attributed to the Sr-doped TiO_2/$SrTiO_3$ heterostructure and the self-doping effect due to the bonding character of Ti-O-Sr.[36]

Table 2. Capacity of dye adsorption of different samples

Dye adsorption amount/mol·cm^{-1}(×10^{-7})	T0	T1	T2	T3
Treating for 0 min	0.42	0.50	0.48	0.44
Treating for 30 min	0.63	0.92	0.88	0.78
Treating for 60 min	0.92	0.98	0.90	0.83

As stated before, the dye adsorption capacity of 1D Sr-doped TiO_2/$SrTiO_3$ nanorod heterostructure arrays is an important factor influencing the photoelectric conversion efficiency of the DSSCs devices. Previous works show that adsorption capacity of N719 molecule on the working electrode can be improved through the functionalization bonding of the hydroxide group onto surface of the electrode material and the carboxyl group of the dye molecule.[37] Accordingly, a hydroxylation functionalization process is performed by soaking the samples in the mixture of deionized water and ammonium hydroxide to enhance the dye loading ability. The dye adsorption capacity test is carried out and the results are shown in Table 3. It is revealed from Table 2 that the amount of loading dye molecular within 60 min almost doubles compared with the untreated samples, demonstrating the functionalization strategy here is effective to increase the dye loading capacity. The dye loading amount increases faster within 30 min, then gets gentle beyond 30 min, showing that at the beginning the bonding reaction between

hydroxide group and carboxyl group is active and subsequently tends to be saturated in a short time.

The J-V characteristics of the DSSC devices based on Sr-doped $TiO_2/SrTiO_3$ heterostructures and rutile TiO_2 are recorded under 1 sun illumination (AM 1.5, 100 mW cm^{-2}), as illustrated in Figure 7. The solar cell parameters are summarized in Table 3. DSSCs based on rutile TiO_2 nanorods array show photoconversion efficiency (η) of 3.10 %, with the open circuit voltage (V_{OC}) of 0.78 V and short current density (J_{SC}) of 6.44 mA cm^{-2}, respectively, so the fill factor (*FF*) was calculated to be 65.9 %. Comparatively, the DSSCs based on T1 heterostructrue sample displays a conversion efficiency of 4.70 %, with J_{SC} = 8.42 mA cm^{-2}, V_{OC} = 0.80 V, and *FF* = 75.5 %. This indicates that the photoelectric conversion efficiency (η) of DSSCs based on the $SrTiO_3$/Sr-doped TiO_2 heterostructures can be greatly enhanced. As the concentration of Sr^{2+} increases for the $SrTiO_3$/Sr-doped TiO_2 heterostructures from T1 to T3, photoelectric conversion efficiency of DSSCs does not increase all the way, the photoelectric conversion efficiency of DSSCs based on T2 and T3 samples is even lower than that of pristine TiO_2 nanorod arrays. This might result from that, with too much $SrTiO_3$ formed, the electronic conductive path along nanorods is gradually destroyed, or excessive $SrTiO_3$ itself serves as the recombination center more than accelerates the carrier separation. Therefore, the quantity of $SrTiO_3$ should be optimized carefully for high conversion efficiency.

Table 3. Photovoltaic parameters of DSSCs based on Sr-doped $TiO_2/SrTiO_3$ heterostructures

Sample	J_{SC} / mA cm^{-2}	V_{OC} / V	*FF* / %	η / %
T0	6.44	0.78	65.9	3.10
T1	8.42	0.80	75.5	4.70
T2	7.37	0.77	65.3	3.55
T3	4.55	0.76	67.4	2.24

As the carrier-recombination may cause significant emission signal in the photoluminescence (PL) spectrum, the transfer behavior of the photogenerated electron-hole pairs can be evaluated. The PL emission spectrum is applied to investigate the separation and transfer process of charge carriers, as well as the trapping behavior of charge carriers. Fig. 8 shows the PL spectra of rutile TiO_2 and Sr-doped $TiO_2/SrTiO_3$ heterostructures. It can be seen that after the heterostructure is formed, the intensity of PL peaks significantly decreases firstly, and with the further increasing concentration of Sr^{2+}, the intensity of PL peak augments gradually. The observed intensity decrement can be ascribed to the decreased recombination rate of photo-generated electron-hole pairs at a low concentration of Sr^{2+}, indicating that the formation of Sr-doped $TiO_2/SrTiO_3$ heterostructures can apparently restrain the recombination of electron-holes pairs. However, further increasing the Sr^{2+} concentration may bring more defect sites (or recombination centers) and oxygen vacancies in the system and, TiO_2 nanorod as carriers transport pathway, the hierarchical structure may be damaged by too high doping-concentration of stromtium, both of which will result in more recombination of photoinduced electrons-holes pairs and relatively stronger PL emission. [31]

To better understand the electrochemical characteristic of the samples, electrochemical impedance spectroscopy (EIS) is applied to describe the charge transfer kinetics at the photoanode interface, as shown in Fig. 8b. All three

samples show two arcs in high frequency and low frequency region. It is reported that the first arc implies the charge-transfer resistance of the electrode, and the diameter of the second arc implies the electron life time.[38, 39] Accordingly, the resistance of the electrode is about 3.4 (T0), 1.5 (T1) and 4.7 (T3) ohm, respectively, which proves that the Sr-doped $TiO_2/SrTiO_3$ heterostructures can effectively improve the charge transfer performance. More importantly, the diameter of the second arcs is in the order of $D_1>D_0>D_3$, demonstrating that Sr-doped $TiO_2/SrTiO_3$ heterostructure can effectively prolong the charge carriers' lifetime, but excess $SrTiO_3$ may result in the counter effect.

The Sr-doping into lattice of TiO_2 could create impurity energy level and narrow the band gap for a wide light absorption. The energy band diagram of DSSCs based on Sr-doped $TiO_2/SrTiO_3$ heterostructure is shown in Fig. 9. Due to the matched band gap energy structure between TiO_2 and $SrTiO_3$, the formation of Sr-doped $TiO_2/SrTiO_3$ heterostructure can effectively suppress the recombination rate of light-induced electrons-holes. The conduction band (CB) of $SrTiO_3$ locates higher position than that of the rutile TiO_2, while the valence band (VB) of $SrTiO_3$ lays lower position than that of rutile TiO_2.[38, 41] Therefore, the photoinduced electrons from the lowest unoccupied molecular orbital (LUMO) of the dye molecule will transfer to the CB of $SrTiO_3$ and immediately transfer to the CB of TiO_2, also the photogenerated holes in TiO_2 can effectively impregnate into the VB of $SrTiO_3$. According to the diagram, if the $SrTiO_3$ layer is too thick, the inputted electrons from dye will take longer time to inject from $SrTiO_3$ to TiO_2, and this increases the recombination rate with the accumulative holes in VB of $SrTiO_3$. Herein, the experiment results agree well with the band gap energy structure. The formation of Sr-doped $TiO_2/SrTiO_3$ heterostructure can effectively prolong the carrier lifetime and the best photoelectric conversion performance can be attained with a proper $SrTiO_3$ layer.

Compared with DSSCs based on conventional sol-gel route synthesized TiO_2 nanoparticles (NP), the DSSCs based on the nanoarray structure can avoid large electron/hole recombination loss. It is generally considered that the sol-gel route synthesized TiO_2 nanoparticle film via spin-coating process on the FTO contain more grain boundaries than the directly grown nanoarray structure. Due to the electron trapping/scattering at grain boundaries, the more grain boundaries in NP films may result in higher energy loss than that of the nanoarray structures. The energy loss in nanoarray structure is about two orders of magnitude higher than that of single crystal. Considering above experimental results, the greatly enhanced power conversion efficiency of the DSSCs based on Sr-doped $TiO_2/SrTiO_3$ heterostructure photoanode can be ascribed to following three aspects. Firstly, the hydroxylation treatment exerts a profound influence on capacity of dye adsorption, and a relatively higher capacity of dye absorbing is in favor of higher photoelectric conversion efficiency. Secondly, the self-doping of Sr into lattice of TiO_2 and the formation of Sr-doped $TiO_2/SrTiO_3$ heterostructure induces the transition of the optical response from ultraviolet region to visible region with a better photo-response performance, which can be confirmed by the UV-vis diffuse reflectance measurements. Thirdly, a uniquely matched bad gap energy structure for Sr-doped $TiO_2/SrTiO_3$ heterostructure can efficiently separate photogenerated charge carriers, and reduce the probability of recombination between electrons and holes, thus results in greatly enhanced photoelectric conversion efficiency.

4. Conclusion

In summary, we demonstrate a greatly enhanced photovoltaic performance of dye-sensitized solar cells based

on Sr-doped TiO_2/$SrTiO_3$ nanorod array heterostructures. The self-doping of stromtium into lattice of TiO_2 and the formation of $SrTiO_3$/Sr-doped TiO_2 heterostructure induces a transition of the optical response from ultraviolet region to visible region with a better photo-response performance. The dye loading capacity on the Sr-doped TiO_2/$SrTiO_3$ nanorod array heterostructures can be improved through the functionalization bonding of the hydroxide group on surface of the electrode material and the carboxyl group of the dye molecule. The photogenerated charge carriers can be effectively separated due to the formation of Sr-doped TiO_2/$SrTiO_3$ heterostructure with uniquely matched bad gap energy structure, and reduce the probability of recombination between electrons and holes, thus results in a greatly enhanced photoelectric conversion efficiency.

Acknowledgements

We acknowledge support from the National Natural Science Funds for Distinguished Young Scholars (51025211), National Nature Science Foundation of China (No. National Nature Science Foundation of China (no. 51272137), the Shandong Natural Science Fund for Distinguished Young Scholars (JQ200915), the Tai Shan Scholar Foundation of Shandong Province.

References

1. B. O'Regan, B. O'Regan and M. Graetzel, *Nature (London)*, 1991, **353**, 737-740.
2. B. C. O'Regan and J. R. Durrant, *Accounts of Chemical Research*, 2009, **42**, 1799-1808.
3. H. J. Koo, Y. J. Kim, Y. H. Lee, W. I. Lee, K. Kim and N. G. Park, *Advanced Materials*, 2008, **20**, 195-199.
4. P.-C. Shih, J.-D. Peng, C.-P. Lee, R. Y.-Y. Lin, T.-C. Chu, R. Vittal and K.-C. Ho, *ChemElectroChem*, 2014, **1**, 532-535.
5. A. Kudo and Y. Miseki, *Chemical Society Reviews*, 2009, **38**, 253-278.
6. Q. Huang, F. Kang, H. Liu, Q. Li and X. Xiao, *Journal of Materials Chemistry A*, 2013, **1**, 2418-2425.
7. Z. Zhang, C.-C. Wang, R. Zakaria and J. Y. Ying, *The Journal of Physical Chemistry B*, 1998, **102**, 10871-10878.
8. J. Ng, S. Xu, X. Zhang, H. Y. Yang and D. D. Sun, *Advanced Functional Materials*, 2010, **20**, 4287-4294.
9. F.-X. Xiao, *ACS applied materials & interfaces*, 2012, **4**, 7055-7063.
10. S. Chai, G. Zhao, P. Li, Y. Lei, Y.-n. Zhang and D. Li, *The Journal of Physical Chemistry C*, 2011, **115**, 18261-18269.
11. W.-Y. Cheng, T.-H. Yu, K.-J. Chao and S.-Y. Lu, *ChemCatChem*, 2014, **6**, 293-300.
12. Y. Wei, J. Jiao, Z. Zhao, W. Zhong, J. Li, J. Liu, G. Jiang and A. Duan, *Journal of Materials Chemistry A*, 2015, 3, 11074-11085.
13. K. Yang, W. Pu, Y. Tan, M. Zhang, C. Yang and J. Zhang, *Materials Science in Semiconductor Processing*, 2014, **27**, 777-784.
14. H. A. Hamedani, N. K. Allam, H. Garmestani and M. A. El-Sayed, *The Journal of Physical Chemistry C*, 2011, **115**, 13480-13486.
15. L. Kumaresan, M. Mahalakshmi, M. Palanichamy and V. Murugesan, *Industrial & Engineering Chemistry Research*, 2010, **49**, 1480-1485.
16. X. Feng, K. Zhu, A. J. Frank, C. A. Grimes and T. E. Mallouk, *Angewandte Chemie*, 2012, **51**, 2727-2730.
17. E. Hendry, M. Koeberg, B. O'Regan and M. Bonn, *Nano Letters*, 2006, **6**, 755-759.
18. B. Liu and E. S. Aydil, *Journal of the American Chemical Society*, 2009, **131**, 3985-3990.
19. M. Xu, P. Da, H. Wu, D. Zhao and G. Zheng, *Nano letters*, 2012, **12**, 1503-1508.
20. Q. Huang, G. Zhou, L. Fang, L. Hu and Z.-S. Wang, *Energy & Environmental Science*, 2011, **4**, 2145-2151.
21. Q. Liu, H. Lu, Z. Shi, F. Wu, J. Guo, K. Deng and L. Li, *ACS applied materials & interfaces*, 2014, **6**, 17200-17207.
22. V. Singh, I. J. C. Beltran, J. C. Ribot and P. Nagpal, *Nano Letters*, 2014, **14**, 597-603.

23. A. Wolcott, W. A. Smith, T. R. Kuykendall, Y. Zhao and J. Z. Zhang, *Small*, 2009, **5**, 104-111.
24. K. Iijima, Y. Tomita, R. Takayama and I. Ueda, *Journal of Applied Physics*, 1986, **60**, 361-367.
25. H. Zheng, J. Wang, S. E. Lofland, Z. Ma, L. Mohaddes-Ardabili, T. Zhao, L. Salamanca-Riba, S. R. Shinde, S. B. Ogale, F. Bai, D. Viehland, Y. Jia, D. G. Schlom, M. Wuttig, A. Roytburd and R. Ramesh, *Science*, 2004, **303**, 661-663.
26. Z.-S. Wang, M. Yanagida, K. Sayama and H. Sugihara, *Chemistry of Materials*, 2006, **18**, 2912-2916.
27. Y. Qin, G. Wang and Y. Wang, *Catalysis Communications*, 2007, **8**, 926-930.
28. Y. Diamant, S. G. Chen, O. Melamed and A. Zaban, *The Journal of Physical Chemistry B*, 2003, **107**, 1977-1981.
29. Y. Jia, S. Shen, D. Wang, X. Wang, J. Shi, F. Zhang, H. Han and C. Li, *Journal of Materials Chemistry A*, 2013, **1**, 7905-7912.
30. M. Ye, M. Wang, D. Zheng, N. Zhang, C. Lin and Z. Lin, *Nanoscale*, 2014, **6**, 3576-3584.
31. D. R. Baker and P. V. Kamat, *Advanced Functional Materials*, 2009, **19**, 805-811.
32. S. Wang, X. Zhang, G. Zhou and Z.-S. Wang, *Physical Chemistry Chemical Physics*, 2012, **14**, 816-822.
33. C. Zha, L. Shen, X. Zhang, Y. Wang, B. A. Korgel, A. Gupta and N. Bao, *ACS applied materials & interfaces*, 2014, **6**, 122-129.
34. T. Cao, Y. Li, C. Wang, C. Shao and Y. Liu, *Langmuir*, 2011, **27**, 2946-2952.
35. C. Wang, Z. Chen, H. Jin, C. Cao, J. Li and Z. Mi, *Journal of Materials Chemistry A*, 2014, **2**, 17820-17827.
36. C. Zhang, S. Chen, L. e. Mo, Y. Huang, H. Tian, L. Hu, Z. Huo, S. Dai, F. Kong and X. Pan, *The Journal of Physical Chemistry C*, 2011, **115**, 16418-16424.
37. A. Subramanian and H.-W. Wang, *Applied Surface Science*, 2012, **258**, 7833-7838.
38. C. W. Kim, S. P. Suh, M. J. Choi, Y. S. Kang and Y. S. Kang, *Journal of Materials Chemistry A*, 2013, **1**, 11820-11827.
39. H. Sun, L. Pan, X. Piao and Z. Sun, *Journal of Materials Chemistry A*, 2013, **1**, 6388-6392.
40. P.-Q. Wang, Y. Bai, J.-Y. Liu, Z. Fan and Y.-Q. Hu, *Catalysis Communications*, 2012, **29**, 185-188.
41. I. Hod, M. Shalom, Z. Tachan, S. Rühle and A. Zaban, *The Journal of Physical Chemistry C*, 2010, **114**, 10015-10018.

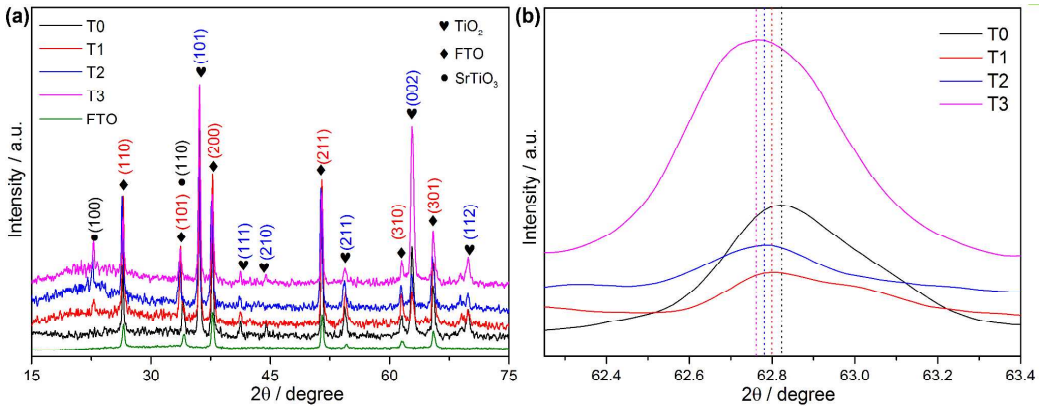

Figure 1. XRD patterns of the Sr-doped $TiO_2/SrTiO_3$ nanorod array heterostucture and the FTO substrate (Initial Sr^{2+} content of 0, 5, 25, 50 mM are titled as T0-T3, and the FTO substrate is titled as FTO).

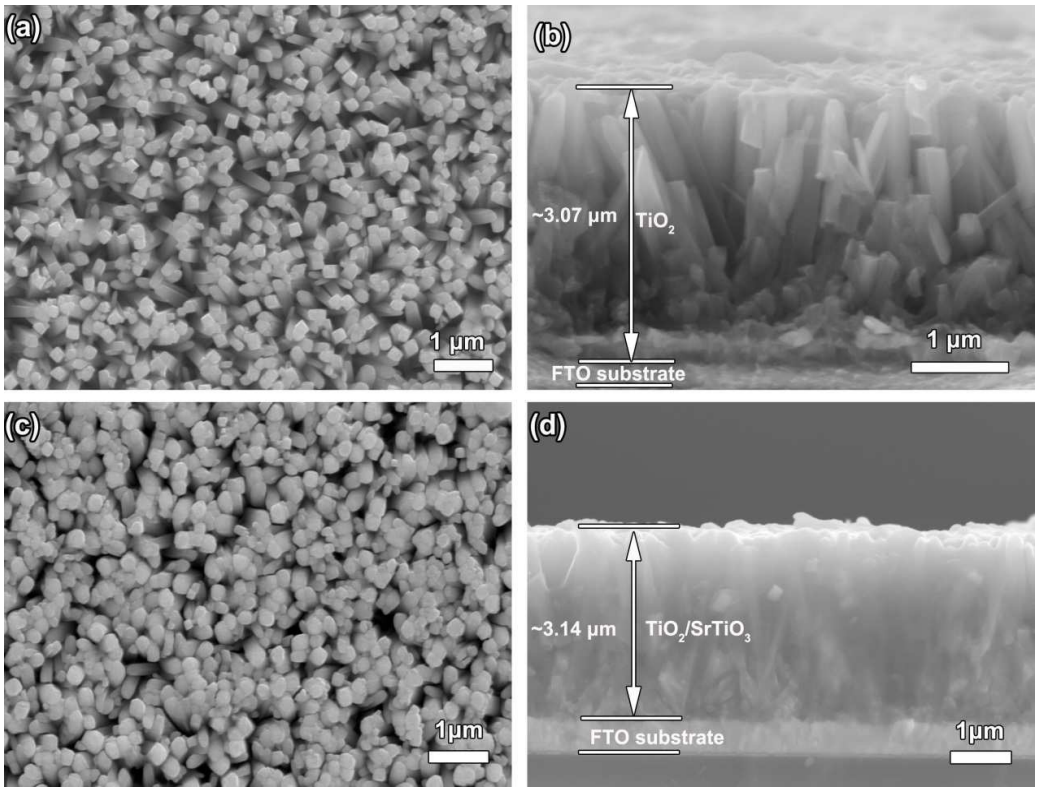

Figure 2. Top view and cross-sectional view SEM images of (a-b) TiO_2 nanorod arrays and (c-d) Sr-doped $TiO_2/SrTiO_3$ nanorod array heterostructures grown on FTO substrate.

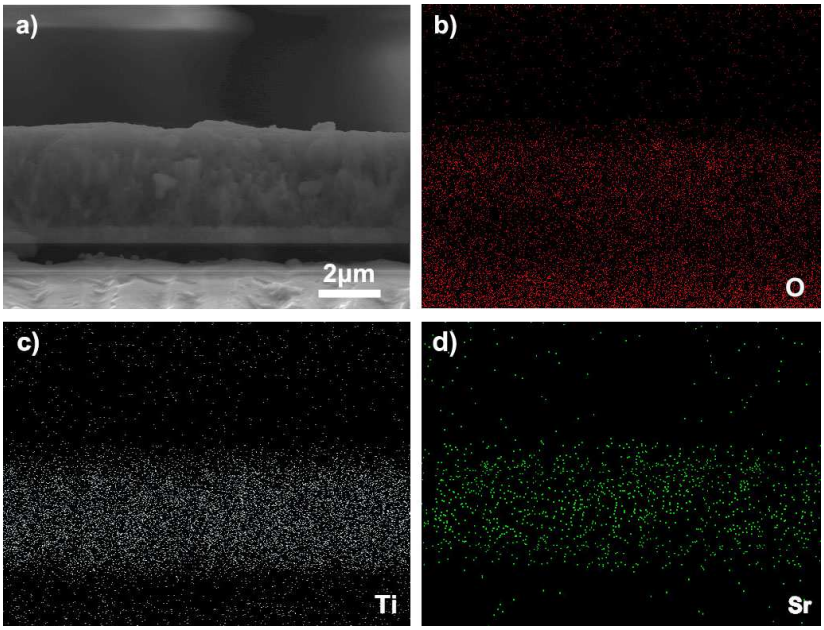

Figure 3. EDS elemental mapping images of Sr-doped $TiO_2/SrTiO_3$ heterostructure (T1).

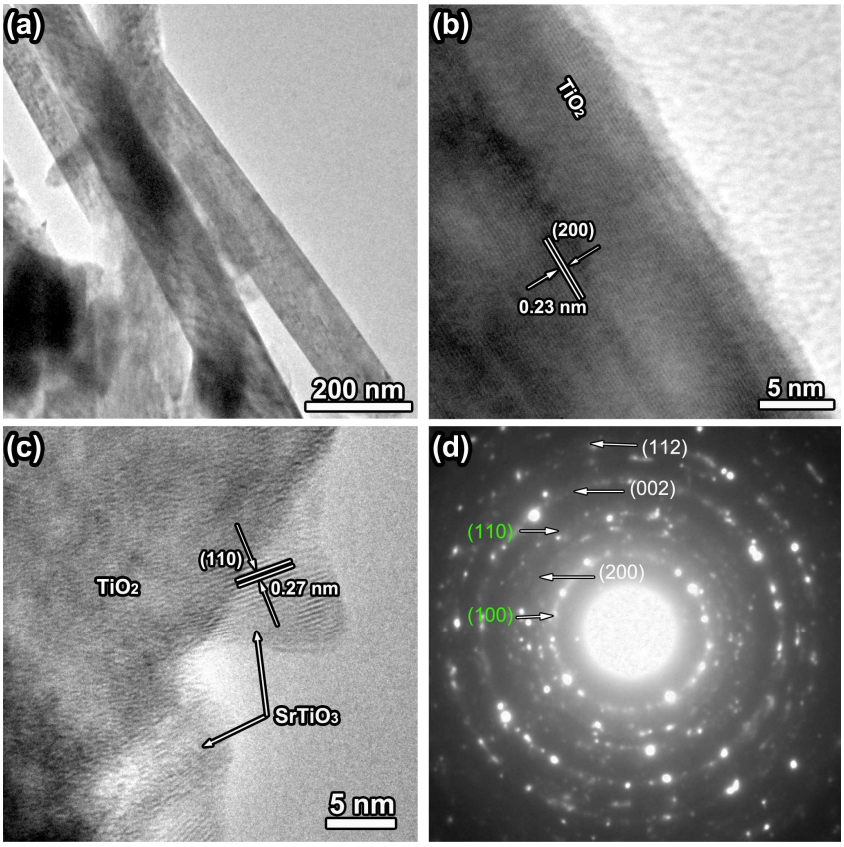

Figure 4. (a-b) Low-magnification TEM image and HRTEM lattice image of rutile TiO_2 nanorod. The marked d-spacing of 0.23 nm corresponds well to (200) plane of rutile TiO_2. (c) A typical HRTEM lattice image of Sr-doped $TiO_2/SrTiO_3$ heterostructure. The marked d-spacing of 0.27 nm corresponds well to that of (110) plane of cubic $SrTiO_3$. (d) Electron diffraction pattern from Sr-doped $TiO_2/SrTiO_3$ heterostructure, the diffraction rings correspond to the (200), (002) and (112) planes of rutile TiO_2, (100) and (110) plane of $SrTiO_3$.

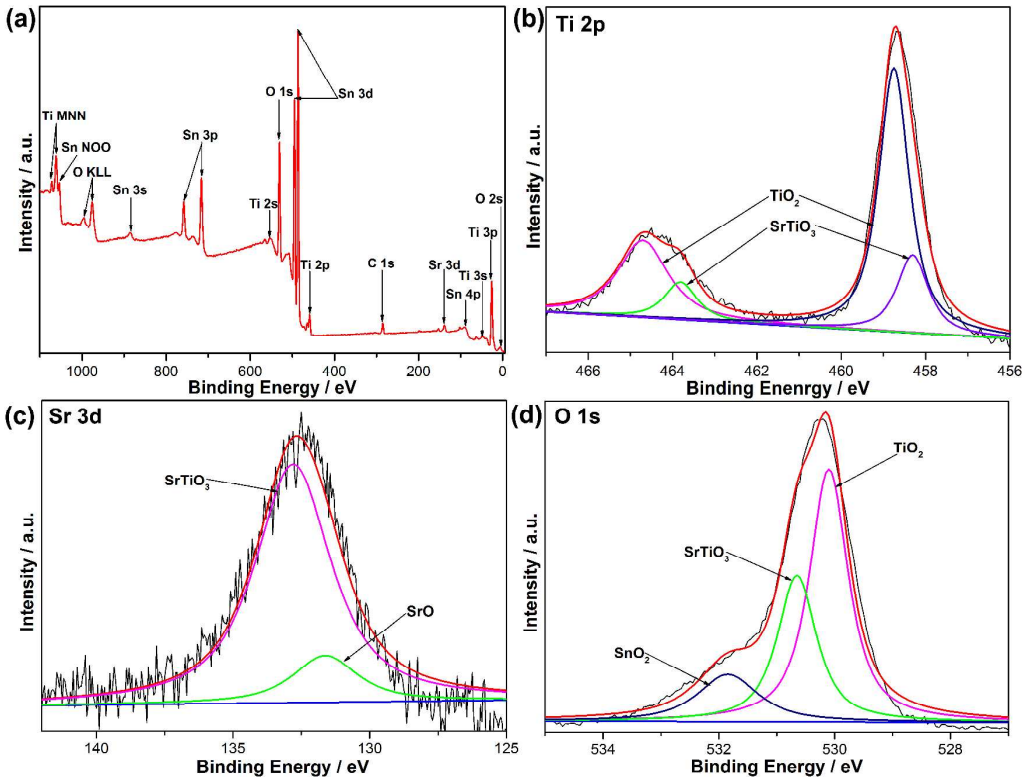

Figure 5. (a) XPS of the Sr-doped $TiO_2/SrTiO_3$ heterostructure (T2), (b) XPS spectra of Ti 2p including Cl $2p_{1/2}$ and Cl $2p_{3/2}$, (c) XPS spectra of Sr 3d, (d) XPS spectra of O 1s.

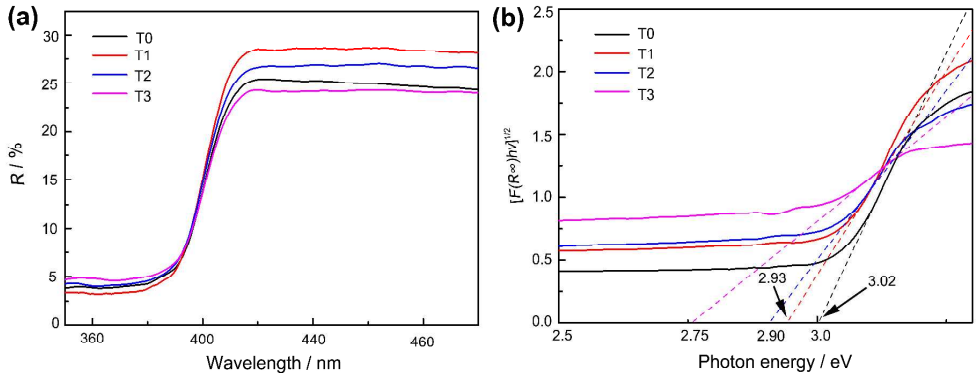

Figure 6. (a) The UV-vis diffusive reflectance spectra (DRS) of the TiO_2 and Sr-doped $TiO_2/SrTiO_3$ heterostructure samples, (b) the plots of transforming Kubelka-Munk function versus the energy of light.

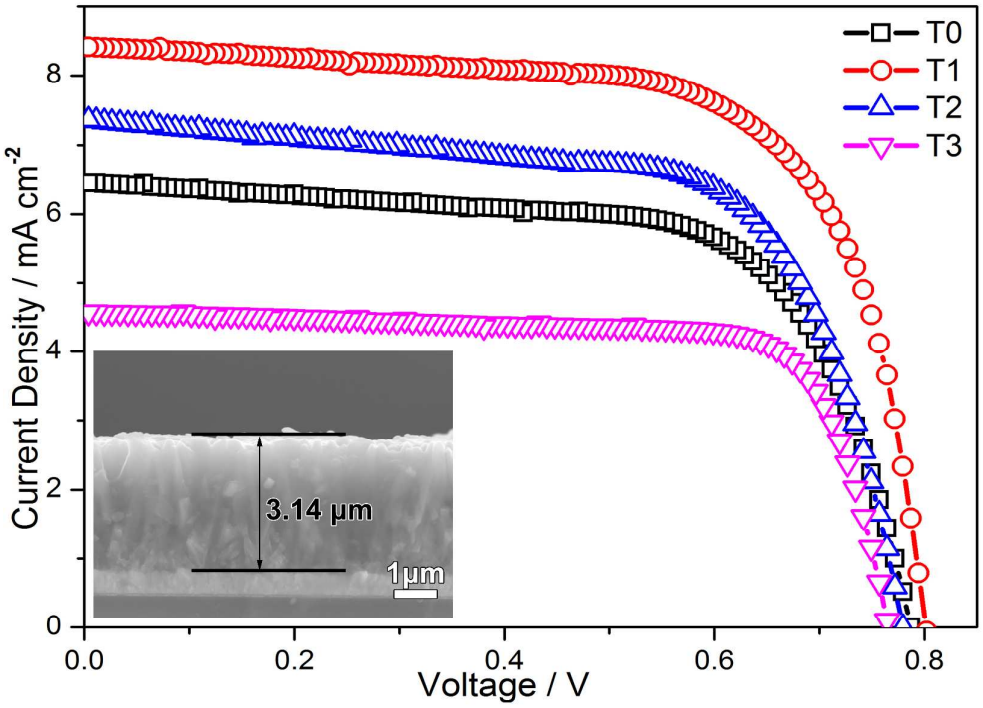

Figure 7. Photocurrent density voltage curves measured under AM 1.5G, at 1 sun light intensity with a shadow mask (Initial Sr^{2+} content of 0, 5, 25, 50 mM are titled as T0-T3 respectively).

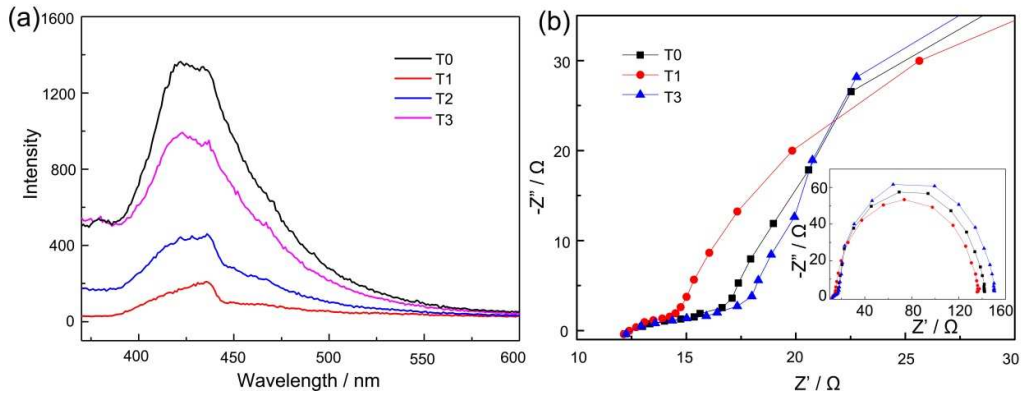

Figure 8. (a) PL spectra of the TiO_2 and Sr-doped $TiO_2/SrTiO_3$ heterostructure samples, (b) Low-resistance scale (10-30 Ω) and full scale (inset graph) Nyquist-plots of pure rutile TiO_2 nanorods (T0) and the Sr-doped $TiO_2/SrTiO_3$ heterostructure samples (T1, T3 refer the sample with initial Sr^{2+} content of 5, 50 mM).

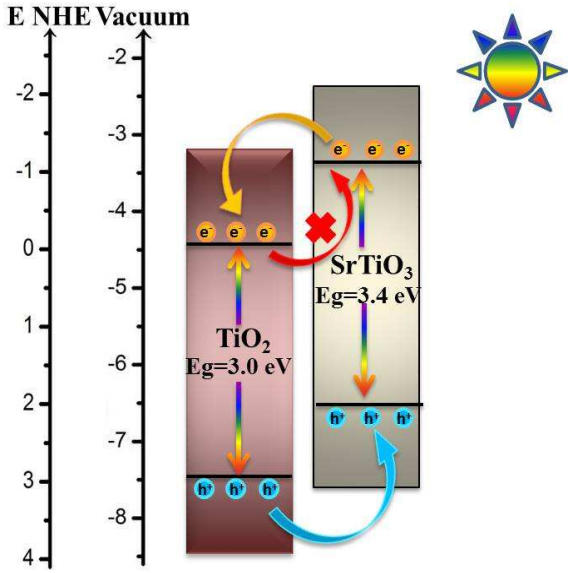

Figure 9. Sketch map of the photo induced charge separation and transfer between $SrTiO_3$ rutile TiO_2 and the energy band structure of the Sr-doped $TiO_2/SrTiO_3$ heterostructure samples.

TOC